Effects of Dispersion of the Dust Velocity in the LISM on the Interstellar Dust Distribution inside the Heliosphere

E. A. Godenko[1, 2, 3*] and V. V. Izmodenov[1, 2, 3]

[1]*Institute for Problems in Mechanics, Russian Academy of Sciences,*
pr. Vernadskogo 101-1, Moscow, 119526 Russia

[2]*Moscow Center for Fundamental and Applied Mathematics, Moscow State University, Moscow, 119992 Russia*

[3]*Space Research Institute, Russian Academy of Sciences, Profsoyuznaya ul. 84/32, Moscow, 117997 Russia*

Abstract—Interstellar dust (ISD) penetrates into the heliosphere due to the relative motion of the Sun and the local interstellar medium (LISM). Inside the heliosphere and at the boundaries, where solar wind interacts with the LISM, distribution of ISD is modified due to the action of the electromagnetic forces, the solar gravitation and the radiation pressure. These forces make the distribution of the ISD particles in the heliosphere inhomogeneous. In previous work we demonstrated the existence of singularities in the ISD density distribution at 0.03−10 AU north and south with respect to the heliospheric current sheet. In this paper we show that dispersion in the ISD velocity distribution strongly affects the singularities. Even small values of dispersion have the drastic impact on the density distribution and smooth the high density layers discovered previously.

INTRODUCTION

The local interstellar medium (LISM) moves relative to the Sun with the speed ∼26 km/s (Witte 2004; McComas 2015). Besides the plasma and neutral components, the LISM also contains dust component (Mann 2010). Unlike the plasma particles, the neutral and dust particles can penetrate into the heliosphere due to the relative motion. For example, the mean free path of neutral hydrogen due to charge exchange is ∼50−100 AU (Izmodenov et al. 2000), comparable with the characteristic size of the heliosphere.

The first evidence for the existence of interstellar particles in the heliosphere was the Lyman-α emission of interstellar neutrals (Bertaux and Blamont 1971). Direct measurements of the interstellar helium atoms were obtained by the Ulysses/GAS instrument (Witte 1992), and since the mean free path of interstellar helium is much larger than the size of the heliosphere, one can derive the macroscopic parameters of the LISM from these measurements. Nowadays, direct measurements of interstellar neutrals (hydrogen, oxygen and helium) are performed on IBEX using the IBEX-Lo instrument (e.g., Moebius

et al. 2009; Katushkina et al. 2015; Baliukin et al. 2017). On the spacecraft SOHO (SWAN instrument) measurements of intensity and spectral characteristics of the Lyman-α emission are continuing (e.g., Quémerais et al. 2013). Various models of the heliosphere are employed for the analysis of the experimental data (e.g., Izmodenov and Alexashov 2015, 2020; Pogorelov et al. 2011; Zirnstein et al. 2016).

The ISD grains are solid grains with characteristic sizes in the range of hundreds of nanometers to microns (Mathis et al. 1977). Chemical composition of ISD is carbonaceous materials and astronomical silicates (Draine 2009). The mass fraction of ISD in the LISM is about 1% (Mann 2010). The ISD grains are charged positively as net effect of different physical processes such as photoelectron and secondary electron emissions. The presence of nonzero electric charge makes the trajectories of ISD more complex than of interstellar neutrals (not taking charge exchange with protons into account).

It is difficult to detect ISD in the heliosphere because of presence of the interplanetary dust, which is emitted from asteroids, comets and other large objects in the Solar system. It is generally supposed that in the undisturbed LISM the interstellar dust is comoving with other components. This assumption

*E-mail: eg24@yandex.ru

was used in order to detect the ISD grains on Ulysses (Grün et al. 1994). Moreover, the trajectory of Ulysses went significantly out of the ecliptic plane and thus it gave the opportunity to relatively easily separate interstellar dust from interplanetary dust, which is located principally in the ecliptic plane (e.g., zodiacal dust). Presence of ISD was also confirmed in the measurements on board the Galileo (Altobelli et al. 2005) and Cassini (Altobelli et al. 2007) spacecraft.

The first models of the ISD distribution in the heliosphere were made by Bertaux and Blamont (1976) and Levy and Jokipii (1976). They studied the distinct influence of the gravitational and electromagnetic forces on the motion of the dust particles in the heliosphere. The next wave of interest in the ISD studying was associated with the Ulysses measurements. Landgraf et al. (2000, 2003) analyzed these measurements using the Monte-Carlo modeling. They considered the combined influence of the gravitational, radiation pressure and electromagnetic forces on the particles in presence of time-dependent solar magnetic field. The ISD distribution and filtration of the dust grains by the magnetic field at the heliospheric boundaries were explored by Czechowski and Mann (2003), Alexashov et al. (2016). Slavin et al. (2012) have built 3D model of the ISD distribution for two opposite phases of the heliospheric magnetic field (focusing and defocusing). It is also taken account of the turbulence of the interstellar magnetic field and dependence of the surface charge potential on the heliocentric distance. Nowadays, the Monte-Carlo method is often used for theoretical studies of ISD. The descriptions and results of the modeling are shown in Sterken at al. (2012, 2019), Strub et al. (2015, 2019). These models are developed from the earlier model of Landgraf et al. (2000) using advanced numerical techniques and taking into account of the newer measurements. Mishchenko et al. (2020) applied a Lagrangian method (see Osiptsov 2000) to discover singularities in the distribution of ISD in the heliosphere. In the simplified stationary case when the heliospheric current sheet is a plane coinciding with the solar equatorial plane they demonstrated the existence of density singularities where the number density is infinite. They showed that the singularities form several dense dust layers for each size of the ISD particles on both sides of the current sheet. These singularities have never been observed in the previous papers studying the dust distribution in the heliosphere by Monte-Carlo simulations because it requires a computational grid with an extremely high spatial resolution. In this paper we use a computational grid with cell size of 10^{-3} AU and for studying local effects near density peculiarities—of 10^{-6} AU.

Mishchenko et al. (2020) used the assumption that the ISD particles have identical velocities in the LISM. Due to the fact that the ISD particles have nonzero electric charge, they interact with the interstellar magnetic field. Fluctuations of the magnetic field lead to acceleration of the charged dust particles (Hoang et al. 2012), that breaks the uniformity in the ISD velocity distribution in the LISM and adds some rather small dispersion. The goal of this paper is to study the influence of dispersion in the velocity distribution of ISD in the LISM on the emergence of the density singularities in the heliosphere. Slavin et al. (2012) also explore dispersion in the undisturbed LISM, but they do not study its influence on the singularities, since the computational grid used is quite coarse (5 AU for each direction).

DESCRIPTION OF THE MODEL

Mathematical Formulation of the Problem

For the description of the ISD motion in the heliosphere we use a kinetic approach. In this way we should calculate the ISD distribution function $f_d(t, \mathbf{r}, \mathbf{v})$. The kinetic equation for $f_d(t, \mathbf{r}, \mathbf{v})$ is:

$$\frac{\partial f_d}{\partial t} + \mathbf{v} \cdot \frac{\partial f_d}{\partial \mathbf{r}} + \mathbf{F} \cdot \frac{\partial f_d}{\partial \mathbf{v}} = 0, \qquad (1)$$

where $\mathbf{F}$ is the sum of forces acting on the dust particles. On the right hand side of (1) we have zero, because in the heliosphere one can neglect collisions between dust grains and their interaction with plasma protons and electrons (Gustafson 1994). In this article we consider the stationary model of the solar magnetic field in the focusing phase, that is why the kinetic equation solution is also stationary, $\frac{\partial f_d}{\partial t} = 0$:

$$\mathbf{v} \cdot \frac{\partial f_d}{\partial \mathbf{r}} + \mathbf{F} \cdot \frac{\partial f_d}{\partial \mathbf{v}} = 0. \qquad (2)$$

Equation (2) requires boundary conditions to obtain a solution. In order to understand how the ISD distribution is modified inside the region of supersonic solar wind, we assume the ISD flow is undisturbed out of the termination shock (TS)—the shock wave that delimits the region of supersonic solar wind in the model of interaction between solar wind and interstellar medium. This helps to understand the modification of the ISD distribution inside the TS as opposed to that in the heliospheric interface (Alexashov et al. 2016). We consider the TS as a sphere with radius r_{TS} and formulate the boundary condition as:

$$f_d(\mathbf{r}, \mathbf{v})|_{r=r_{\text{TS}}, \mathbf{v} \cdot \mathbf{e}_n > 0} = f_{\text{TS}}(\mathbf{v}), \qquad (3)$$

where $f_{\text{TS}}(\mathbf{v})$ is the ISD distribution function at the TS and $\mathbf{e}_n$ is the interior unit normal to the sphere.
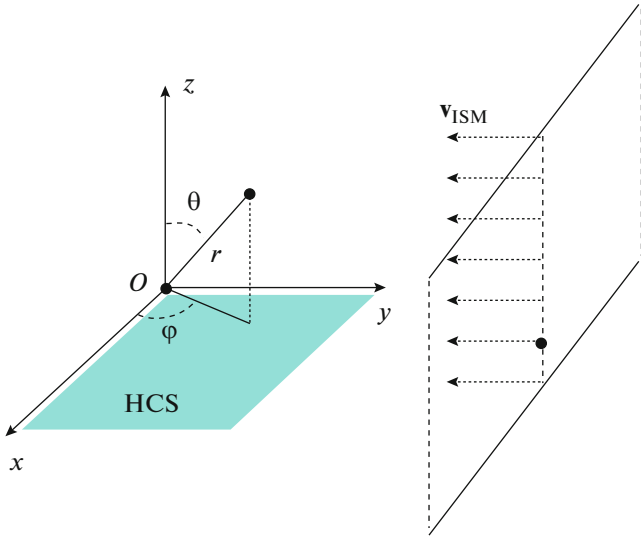
Fig. 1. The coordinate system. The Sun is located at O, the velocity of the LISM $\mathbf{v}_{\text{ISM}}$ is collinear to the Oy axis. The Oz axis coincides with the solar rotation axis. Spherical coordinates are introduced in the standard way.

Below we discuss the form of function $f_{\text{TS}}(\mathbf{v})$ in more detail.

To complete the correct mathematical formulation of the problem we should also set the boundary condition in the velocity space:

$$f_d(\mathbf{r}, \mathbf{v})|_{v \to \infty} = 0. \tag{4}$$

Note that each specific problem described by the formulation (2)–(4) is determined by a specific expression for the force term $\mathbf{F}(\mathbf{r}, \mathbf{v})$ and for the boundary condition function $f_{\text{TS}}(\mathbf{v})$.

Force Analysis

Consider the Cartesian coordinate system as shown in Fig. 1. Katushkina and Izmodenov (2019) provided the analysis of forces acting on the ISD particles. Four main forces act on the particles: the gravitational force $\mathbf{F}_{\text{grav}}$, the radiation pressure force $\mathbf{F}_{\text{rad}}$, the drag force $\mathbf{F}_{\text{drag}}$ due to the interaction of dust grains with protons, electrons and neutrals and the electromagnetic force $\mathbf{F}_{\text{el}}$. Estimates show (Gustafson 1994) that in the heliosphere we can neglect the drag force.

The expression for the gravitational force $\mathbf{F}_{\text{grav}}$ is:

$$\mathbf{F}_{\text{grav}} = -\frac{GM_\odot}{r^2}\mathbf{e}_r, \tag{5}$$

where G is the gravitational constant, $M_\odot$ is the mass of the Sun.
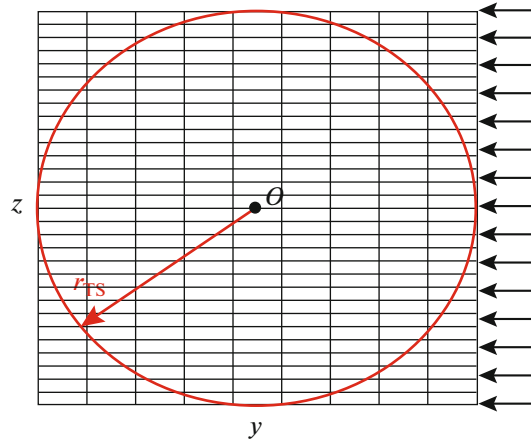
Fig. 2. Computational domain is a square with the side $2\hat{r}_{\text{TS}} = 2\dfrac{r_{\text{TS}}}{L_1}$ described around the circumference of radius $\hat{r} = \hat{r}_{\text{TS}}$ in the $\hat{x} = 0$ plane, where r_{TS} is the distance from the Sun to the TS. The cells of the computational domain are rectangles $\Delta\hat{y} \times \Delta\hat{z}$.

Since $\mathbf{F}_{\text{grav}}$ is parallel $\mathbf{F}_{\text{rad}}$ and both are proportional to r^{-2} it is convenient to introduce the parameter β:

$$\beta = \frac{|\mathbf{F}_{\text{rad}}|}{|\mathbf{F}_{\text{grav}}|}. \tag{6}$$

In this paper for the sake of simplicity we consider spherical particles. In this case β depends only on the star characteristics and particle mass m (see e.g., Katushkina and Izmodenov 2019). Here we use the $\beta = \beta(m)$ curve from Sterken et al. (2012) (green solid line in Fig. 14). The resulting expression for the radiation pressure force is:

$$\mathbf{F}_{\text{rad}} = \beta\frac{GM_\odot}{r^2}\mathbf{e}_r. \tag{7}$$

The magnetic field lines are frozen in the solar wind, that is why if we consider the reference frame related to the solar wind, one can derive the expression for the electromagnetic force using relative (with respect to the solar wind) velocity $\mathbf{v}_{\text{rel}}$ of dust particles:

$$\mathbf{F}_{\text{el}} = \frac{q}{c_0 m_d}\left(\mathbf{v}_{\text{rel}} \times \mathbf{B}\right), \tag{8}$$

where $\mathbf{v}_{\text{rel}} = \mathbf{v} - \mathbf{v}_p$ is the dust particle velocity with respect to the solar wind, q is the particle charge, c_0 is the speed of light, m_d is the dust grain mass, $\mathbf{v}_p$ is the solar wind velocity, $\mathbf{B}$ is the solar magnetic field. The particle charge is expressed through the surface potential U_d and the radius a: $q = U_d a$, and we consider U_d as constant in the supersonic solar wind (Fig. 2 from Alexashov et al. 2016, Fig. 2 from Slavin et al. 2012). Out of the region of the supersonic solar wind one should take account of the changes in value of

surface potential, but it is beyond the scope of the present work. The dust grain mass $m_{\mathrm{d}} = \frac{4}{3}\rho_{\mathrm{d}}\pi a^3$, where ρ_{d} is the mass density of dust (here we consider astronomical silicates). We further assume uniform spherically symmetric solar wind: $\mathbf{v}_p = v_{\mathrm{sw}}\mathbf{e}_r$, and for the solar magnetic field we use Parker's model:

$$B_r = \pm B_{\mathrm{E}}\left(\frac{r_E}{r}\right)^2,$$
$$B_\phi = \mp\frac{B_{\mathrm{E}}\Omega r_{\mathrm{E}}}{v_{\mathrm{sw}}}\left(\frac{r_{\mathrm{E}}}{r}\right)\sin\theta,$$
$$B_\theta = 0, \qquad (9)$$

where B_{E} is the averaged solar magnetic field magnitude at the Earth's orbit, r_{E} is the astronomical unit, Ω is the angular velocity of solar rotation. The sign $\pm$ denotes the change in the polarity of the magnetic field across the heliospheric current sheet (HCS). Here for simplicity we assume a planar shape of the HCS (plane Oxy in Fig. 1). In reality there is a non-zero angle between the solar rotation axis and the magnetic axis, so the HCS has the "ballerina skirt" shape. Here we also assume that the heliospheric magnetic field is stationary: that is, the HCS plane is at rest and in the region $z > 0$ magnetic field components $B_r < 0$, $R_\varphi > 0$ and vice versa. That is, we ignore the 22-year solar cycle that leads to polarity changes every 11 years, accompanied by changes in the geometry of the HCS. In future we plan to expand our model to the time-dependent magnetic field case.

Thus, the expression for $\mathbf{F}(\mathbf{r}, \mathbf{v})$ is:

$$\mathbf{F}(\mathbf{r}, \mathbf{v}) = (\beta - 1)GM_s \cdot \frac{\mathbf{e}_r}{r^2}$$
$$+ \frac{q}{c_0 m_{\mathrm{d}}}((\mathbf{v} - \mathbf{v}_p) \times \mathbf{B}). \qquad (10)$$

Boundary Condition

Let us assume that in the LISM there is a flux of the ISD particles with the average velocity $\mathbf{v}_{\mathrm{ISM}}$ and dispersion of the v_z velocity component. The interstellar magnetic field has spatial and temporal inhomogeneties which act as sources for the acceleration of ISD particles (Hoang et al. 2012). This acceleration is the reason for the variations in the velocities of individual dust particles and, therefore, appearance of dispersion in the ISD velocity distribution. Below we demonstrate that relatively small values of dispersion just of the v_z velocity component significantly influence the results. Then the expression for $f_{\mathrm{TS}}(\mathbf{v})$ is:

$$f_{\mathrm{TS}}(\mathbf{v}) = n_{\mathrm{ISM}}\delta(v_x)\delta(v_y + v_{\mathrm{ISM}})$$
$$\times \frac{1}{\sigma_z\sqrt{2\pi}}\exp\left(-\frac{v_z^2}{2\sigma_z^2}\right), \qquad (11)$$

where δ is the Dirac delta-function, σ_z is the dispersion of the v_z velocity component. For $\sigma_z \to 0$ the expression (11) degenerates into the singular distribution function for the case when all dust particles have the identical velocity $\mathbf{v}_{\mathrm{ISM}}$:

$$f_{\mathrm{TS}}(\mathbf{v}) = n_{\mathrm{ISM}}\delta(v_x)\delta(v_y + v_{\mathrm{ISM}})\delta(v_z), \qquad (12)$$

and the formulation of the problem is identical to the one given by Mishchenko et al. (2020).

Slavin et al. (2012) take account of the dispersion by addition of the supplementary velocity component, lying in the plane, perpendicular to the direction of the interstellar magnetic field. This supplementary velocity component has constant absolute value (3 km/s) and random direction in the mentioned plane. In the present work we just model the dispersion of the v_z velocity component using the normal distribution.

Dimensionless Formulation of the Problem

As a characteristic distance we consider $L_1 = \frac{GM_\odot}{v_{\mathrm{ISM}}^2}$ and as a characteristic velocity—v_{ISM}. Since the problem is linear and homogeneous in $f_{\mathrm{d}}(\mathbf{r}, \mathbf{v})$ we can substitute $f_{\mathrm{d}} \to \frac{f_{\mathrm{d}}}{n_{\mathrm{ISM}}}$ and eliminate n_{ISM} in (11). Dimensionless formulation of the problem (2)–(4), (10), (11) is:

$$\begin{cases} \hat{\mathbf{v}} \cdot \frac{\partial \hat{f}_{\mathrm{d}}}{\partial \hat{\mathbf{r}}} + \hat{\mathbf{F}} \cdot \frac{\partial \hat{f}_{\mathrm{d}}}{\partial \hat{\mathbf{v}}} = 0 \\ \hat{f}_{\mathrm{d}}(\hat{\mathbf{r}}, \hat{\mathbf{v}})|_{\hat{r} = \hat{r}_{\mathrm{TS}}}, \quad \hat{\mathbf{v}} \cdot \mathbf{e}_n > 0 = \delta(\hat{v}_x)\delta(\hat{v}_y + 1)\frac{1}{\hat{\sigma}_z\sqrt{2\pi}}\exp\left(-\frac{\hat{v}_z^2}{2\hat{\sigma}_z^2}\right) \\ \hat{f}_{\mathrm{d}}(\hat{\mathbf{r}}, \hat{\mathbf{v}})|_{\hat{v} \to \infty} = 0, \end{cases} \qquad (13)$$

where $\hat{\mathbf{r}} = \frac{\mathbf{r}}{L_1}, \hat{\mathbf{v}} = \frac{\mathbf{v}}{v_{\mathrm{ISM}}}, \hat{f}_{\mathrm{d}} = \frac{f_{\mathrm{d}}}{v_{\mathrm{ISM}}^3}, \hat{\mathbf{F}} = \frac{\mathbf{F}L_1}{v_{\mathrm{ISM}}^2}, \hat{\sigma}_z = \frac{\sigma_z}{v_{\mathrm{ISM}}}, \hat{r}_{\mathrm{TS}} = \frac{r_{\mathrm{TS}}}{L_1}$. The expression for the sum of forces (10) in the dimensionless form is:

$$\hat{\mathbf{F}} = (\beta - 1)\frac{\mathbf{e}_r}{\hat{r}^2} + \mathrm{sgn}(\hat{z})\frac{v_{\mathrm{em}}^2}{v_{\mathrm{ISM}}^2}\left(\frac{v_{\mathrm{ISM}}}{v_{\mathrm{sw}}}\hat{\mathbf{v}} - \mathbf{e}_r\right)\left(-\frac{L_\Omega}{L_1}\frac{\mathbf{e}_r}{\hat{r}^2} + \frac{\sin\theta}{\hat{r}}\mathbf{e}_\varphi\right), \qquad (14)$$

with $L_\Omega = \dfrac{v_{sw}}{\Omega}$, $v_{em}^2 = \dfrac{qB_E\Omega r_E^2}{c_0 m_d}$. The dimensionless formulation of the problem contains five dimensionless parameters:

$$\hat{\sigma}_z, \beta, \varepsilon = \frac{v_{em}^2}{v_{ISM}^2}$$

$$= \frac{3U_d B_E R_E^2 \Omega}{4\pi c_0 \rho_d a^2 v_{ISM}^2}, \frac{v_{ISM}}{v_{sw}}, \frac{L_\Omega}{L_1}. \qquad (15)$$

Trajectories in the Plane of Symmetry

Let us consider the projection of the force $\hat{\mathbf{F}}$ on the x-axis:

$$\hat{F}_x = (\beta - 1)\frac{\hat{x}}{\hat{r}^3} + \text{sgn}(\hat{z})\varepsilon\frac{\hat{x}\hat{z}}{\hat{r}^3}$$

$$+ \text{sgn}(\hat{z})\varepsilon\frac{v_{ISM}}{v_{sw}}\left(-\frac{L_\Omega}{L_1}\frac{\hat{v}_y\hat{z} - \hat{v}_z\hat{y}}{\hat{r}^3} - \frac{\hat{v}_z\hat{x}}{\hat{r}^2}\right). \quad (16)$$

Since $\dfrac{v_{ISM}}{v_{sw}} \approx 0.05 \ll 1$, one can neglect the corresponding term, and the expression for $\hat{F}_x$ in simplified form is:

$$\hat{F}_x = (\beta - 1)\frac{\hat{x}}{\hat{r}^3} + \text{sgn}(\hat{z})\varepsilon\frac{\hat{x}\hat{z}}{\hat{r}^3}. \qquad (17)$$

Therefore, dust particles with initial parameters:

$$\hat{x}|_{TS} = 0, \quad \hat{v}_x|_{TS} = 0 \qquad (18)$$

cannot leave the plane $\hat{x} = 0$ under the action of the force (17) according to Picard's existence and uniqueness theorem. In this article for simplicity we consider only such trajectories.

Monte-Carlo Approach

To solve the kinetic equation we use the Monte-Carlo method. The computational domain is divided into rectangular cells $\Delta\hat{y} \times \Delta\hat{z}$ (Fig. 2) and $\Delta\hat{z} \ll \Delta\hat{y}$, because the singular layers found in Mishchenko et al. (2020) are oriented horizontally. Moreover, since their thickness approaches zero one should decrease $\Delta\hat{z}$ in order to detect these peculiarities by Monte-Carlo modeling.

For a dust particle we generate randomly its initial velocity and position on the sphere with radius $r = r_{TS}$ according to the distribution function $f_{TS}(\mathbf{v})$ from (13). During the particle motion in the heliosphere we record the time t_i, which the particle held in the computational domain cells ($t_i = 0$ if particle does not cross the corresponding cell). Then, by kinetic definition of the distribution function and density, and law of large numbers we have:

$$\frac{\hat{F}_0}{N}\sum_{i=1}^{N}\frac{t_i}{\Delta\hat{r}_c\Delta\hat{v}_c} \to f_d(\hat{\mathbf{r}}_c, \hat{\mathbf{v}}_c), \qquad (19)$$

$$\frac{\hat{F}_0}{N}\sum_{i=1}^{N}\frac{t_i}{\Delta\hat{r}_c} \to n_d(\hat{\mathbf{r}}_c), \qquad (20)$$

where N is the number of simulated particles, $\hat{\mathbf{r}}_c$, $\hat{\mathbf{v}}_c$ are the coordinates of the cell center in the phase space, $\Delta\hat{\mathbf{r}}_c$ is the cell volume in the physical space, $\Delta\mathbf{r}_c\Delta\mathbf{v}_c$ is the cell volume in the phase space, $\hat{F}_0$ is the flux of the dust particles through the outer surface per unit of time in dimensionless form:

$$\hat{F}_0 = \int_{-\frac{\pi}{2}}^{\frac{\pi}{2}}\left(\int_{(\hat{\mathbf{v}}\cdot\mathbf{e}_n)>0}(\hat{\mathbf{v}}\cdot\mathbf{e}_n)\,\hat{f}_{TS}(\hat{\mathbf{v}})d\hat{\mathbf{v}}\right)$$

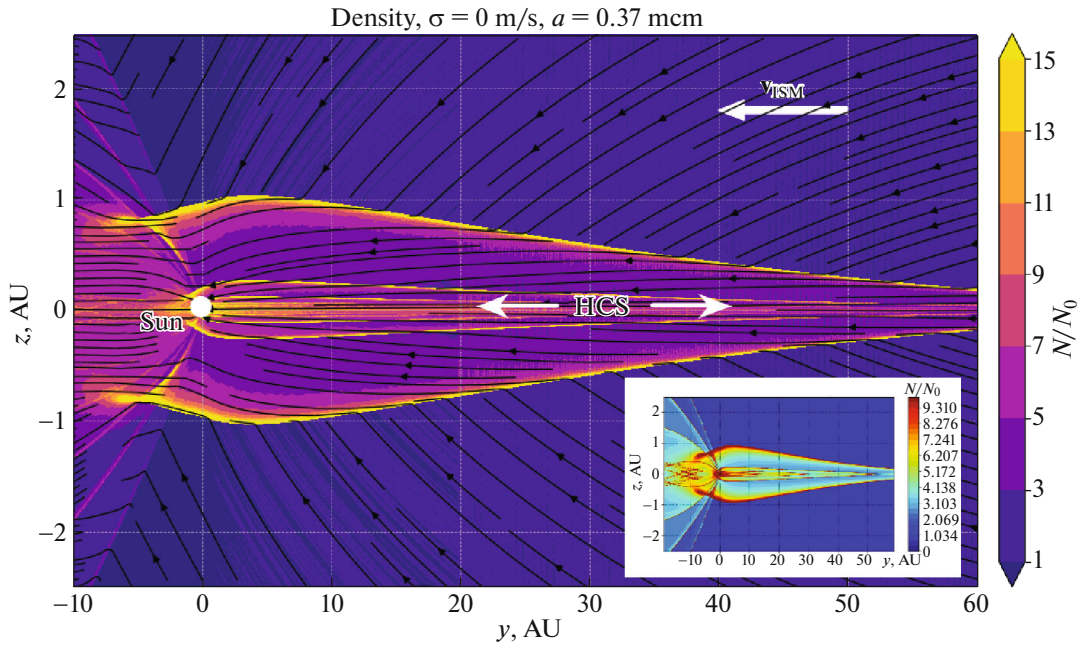$$\times \hat{r}_{TS}d\varphi = 2\hat{r}_{TS} \qquad (21)$$

Technical Characteristics

In this paper we consider particles with the radius $a = 0.37$ μm. For these particles $\beta = 1$ and consequently the gravitational and radiation pressure forces cancel out in (14).

For computations we use the following values of the parameters: $r_{TS} = 100$ AU, $v_{ISM} = 26.4$ km/s, $M_\odot = 2 \times 10^{30}$ kg, $v_{sw} = 400$ km/s, $\Omega = 2.9 \times 10^{-6}$ 1/s, $U_d = +3$ V, $B_E = 30$ μG, $R_E = 1$ AU, $\rho_d = 2500$ kg/m^3.

For all pictures with results in this paper, unless otherwise specified, the cell size inside the computational domain is 0.1×0.001 AU in the Oy and Oz directions respectively. To solve the system of ODEs for a particle's trajectory the fourth order Runge–Kutta method was used.

Note that selected fixed location of the HCS corresponds to the case all ISD particles attract to the HCS (focusing phase). In order to understand it let us consider the z-axis projection of (14):

$$\hat{F}_z = (\beta - 1)\frac{\hat{z}}{\hat{r}^3} + \text{sgn}(\hat{z})\varepsilon\left(-\frac{\hat{x}^2 + \hat{y}^2}{\hat{r}^3}\right.$$

$$+ \frac{v_{ISM}}{v_{sw}}\left(-\frac{L_\Omega}{L_1}\frac{\hat{v}_x\hat{y} - \hat{v}_y\hat{x}}{\hat{r}^3}\right.$$

$$\left.\left. + \frac{\hat{v}_x\hat{x} + \hat{v}_y\hat{y}}{\hat{r}^2}\right)\right), \qquad (22)$$

Fig. 3. Map of the density distribution in the plane $x = 0$ in the case without dispersion. Yellow color envelopes correspond to caustics. Relative statistical error is limited by $2-3\%$ at each point. Number of trajectories $N = 2\,000\,000$. For the sake of comparison, the panel at the right bottom presents the results of Mishchenko et al. (2020) obtained for the same conditions. Radius of particles is $0.37\ \mu$m.
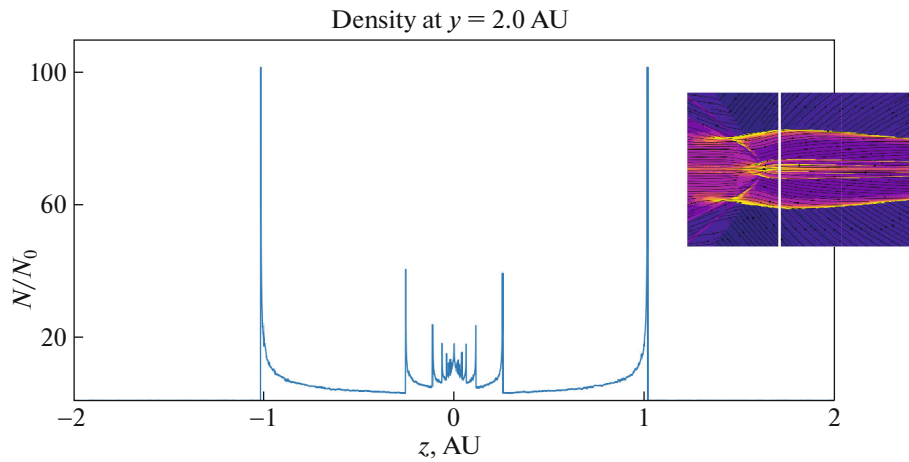
Fig. 4. Distribution of ISD density along line $(x = 0, y = 2)$. The cell size is 0.1×0.001 AU. Relative statistical error is limited by $2-3\%$ at each point. Number of trajectories $N = 2\,000\,000$. Radius of particles is $0.37\ \mu$m.

where again $\dfrac{v_{\mathrm{ISM}}}{v_{\mathrm{sw}}} \approx 0.05 \ll 1$, that is why at the large heliospheric distances the lead term is:

$$-\mathrm{sgn}(\hat{z})\varepsilon \frac{\hat{x}^2 + \hat{y}^2}{\hat{r}^3}. \qquad (23)$$

It is seen, that in the case $\hat{z} > 0$ the z-axis result force component $\hat{F}_z < 0$, so the ISD particles are attracted to the HCS. In the case $\hat{z} < 0$ here is $\hat{F}_z > 0$.

RESULTS

Singularities in Density

It was shown by Mishchenko et al. (2020) that in the case of zero dispersion the ISD trajectories form *caustics* at which the number density of the interstellar dust is infinite. Caustic is the envelope of the ISD trajectories. By its definition, every segment of caustic is tangent to an infinite number of the ISD trajectories, that is the reason of density singularities origin. The distribution of the dust density has
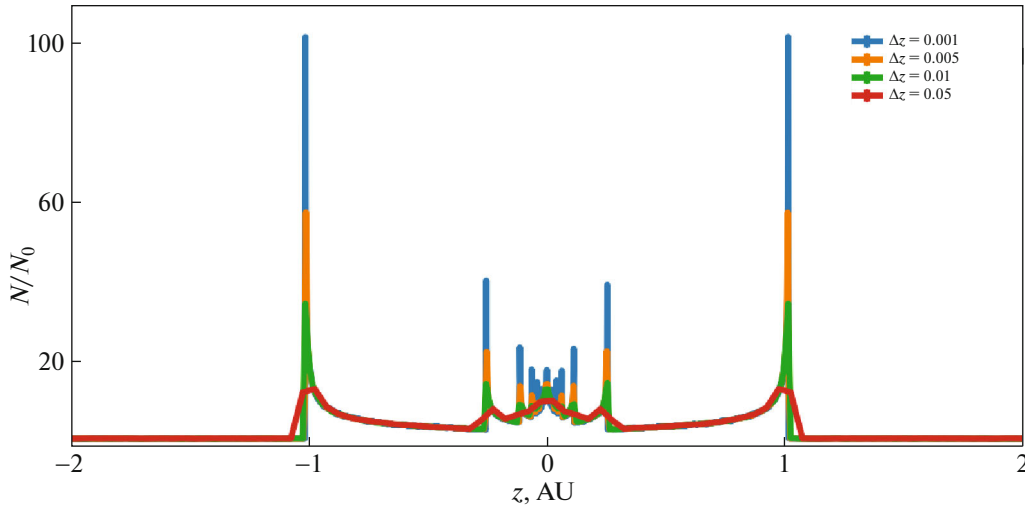
Fig. 5. The ISD density distribution along the same line as in Fig. 4. Four lines of different colour correspond to the different cell size in z-direction ($\Delta y = 0.1$ AU, $\Delta z = \{0.05, 0.01, 0.005, \text{ and } 0.001 \text{ AU}\}$). Relative statistical error is limited by 2−3% at each point. Number of trajectories $N = 2\,000\,000$. Radius of particles is 0.37 μm.
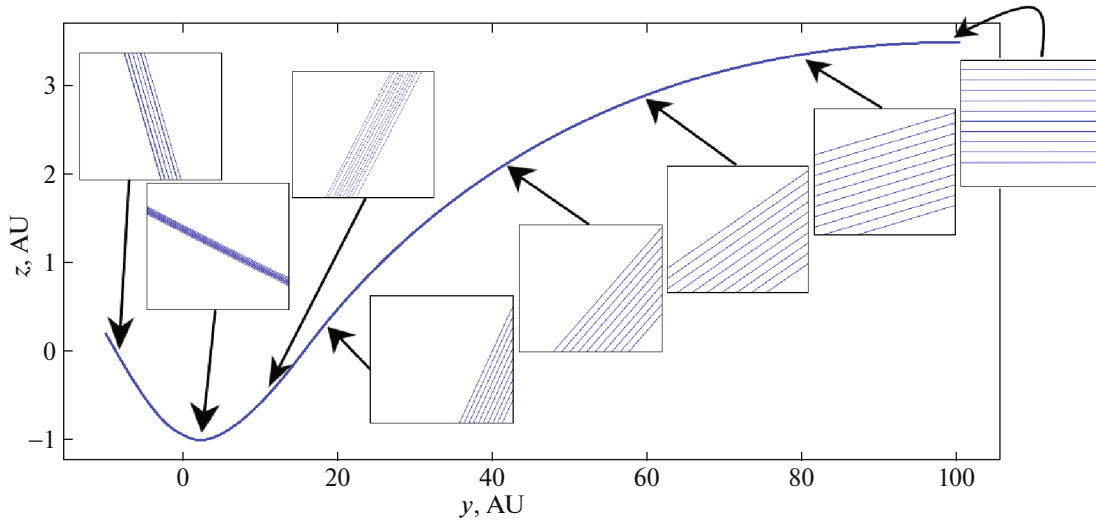
Fig. 6. Tube of trajectories from a small region at the outer boundary. The tube is compressed up to a thousand times at small heliocentric distances. The point of minimal width corresponds to a point on the caustic. Small boxes demonstrate trajectories view at a large scale. Box sizes are 0.6×0.025 AU Radius of particles is 0.37 μm.

multiple singularities. This result was obtained by a Lagrangian approach. In this Section we demonstrate that the singularities can be also obtained by the Monte-Carlo approach (although, perhaps, at the cost of computational efficiency).

Figure 3 shows the map of the ISD density distribution as well as the ISD streamlines. The map shows the region in the vicinity of the HCS. Symmetrical yellow lines in Fig. 3 are the above-mentioned caustics. In the case of Monte-Carlo simulation they represent the thin regions where a sharp density peak is found (Fig. 4). Inside the area delimited by the caustics there is a complex structure of the ISD density distribution with many local peaks.

Since the computational domain consists of finite size cells, high spatial resolution of the numerical grid is required to detect the density singularities with high precision by Monte-Carlo simulations. Figure 5 shows how the ISD density distribution along the line ($x = 0, y = 2$) changes with variation of cell size Δz. The ISD density in cells containing caustic points increases with decreasing of Δz and, therefore, the ISD density singularities located in these cells.

The simple explanation for the formation of the caustics is as follows. Let us look at the particles originating from a small region on the boundary of the computational domain (Fig. 6). This flux tube is compressed with decreasing heliocentric distance and
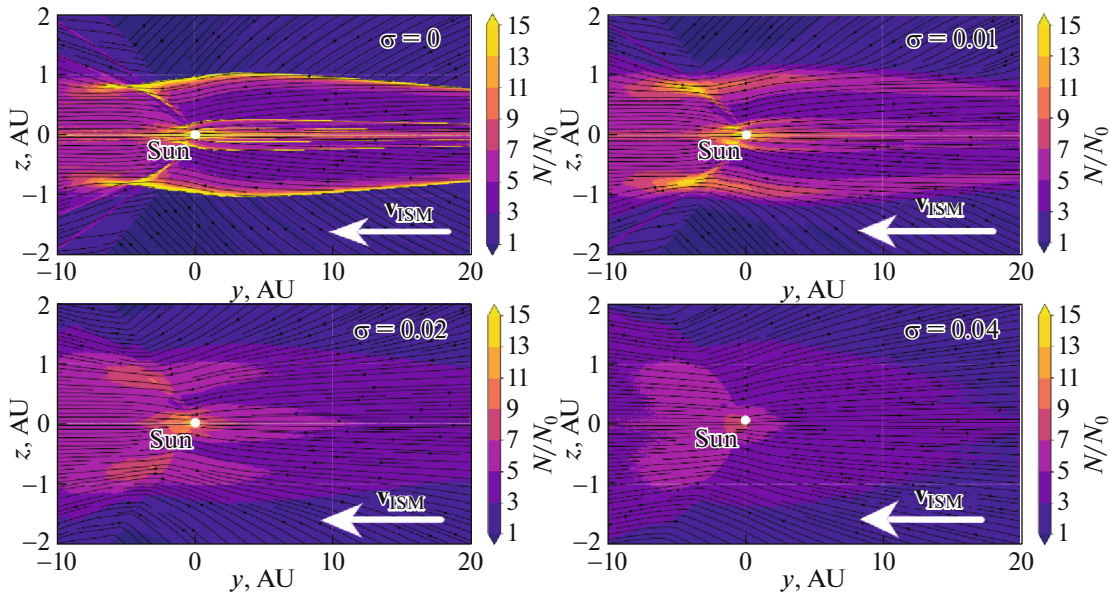
Fig. 7. Comparison of the maps of the ISD density distributions with different dispersion $\hat{\sigma}_z$: 0, 0.01, 0.02, 0.04. With increasing dispersion $\hat{\sigma}_z$ the caustics are smeared and the density singularities disappear. Relative statistical error is limited by 2−3% at each point. Number of trajectories $N = 2\,000\,000$. Radius of particles is 0.37 μm.
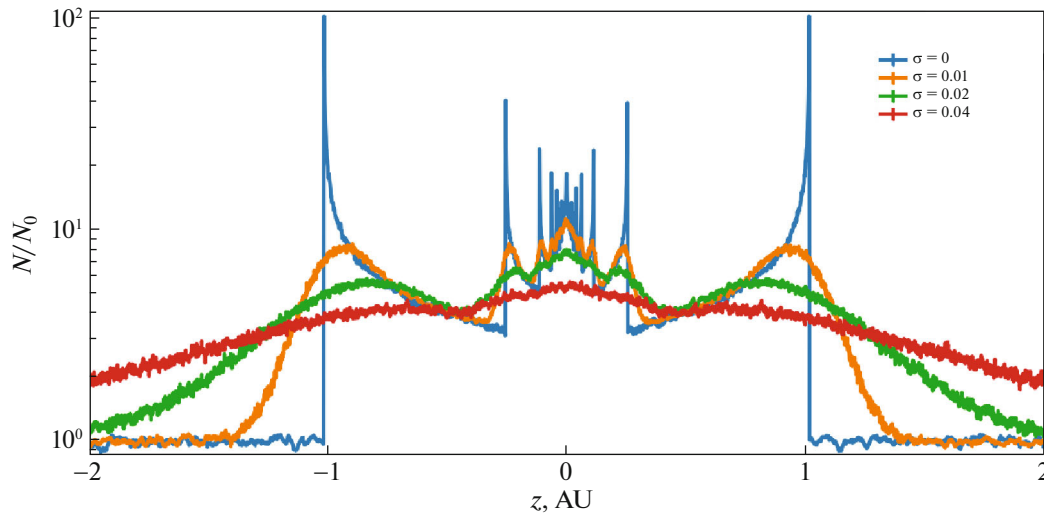
Fig. 8. Comparison of the ISD density distributions along the line ($x = 0$, $y = 2$) with different dispersion $\hat{\sigma}_z$: 0, 0.01, 0.02, 0.04. The structure of density distribution changes drastically with variation of dispersion. Relative statistical error is limited by 2−3% at each point. Number of trajectories $N = 2\,000\,000$. Radius of particles is 0.37 μm.

reaches its minimal width (approaching zero) exactly at the caustic points. From the mass conservation law

$$n_1 v_1 \Sigma_1 = n_2 v_2 \Sigma_2$$

the density n reaches its maximum value at the point where the width Σ is minimal, because v (the velocity component along the y axis) is virtually constant along the trajectory.

Effects of Velocity Dispersion

In this paper we consider mainly the dispersion of the v_z velocity component. We do not consider the dispersion of the v_x velocity component at all because we only study the plane of symmetry $x = 0$, and Fig. 11 shows that dispersion of the v_y velocity component has less impact on the density distribution than dispersion of the v_z velocity component.

To explore the effect of velocity dispersion we performed the calculations for the set of $\hat{\sigma}_z$ values:
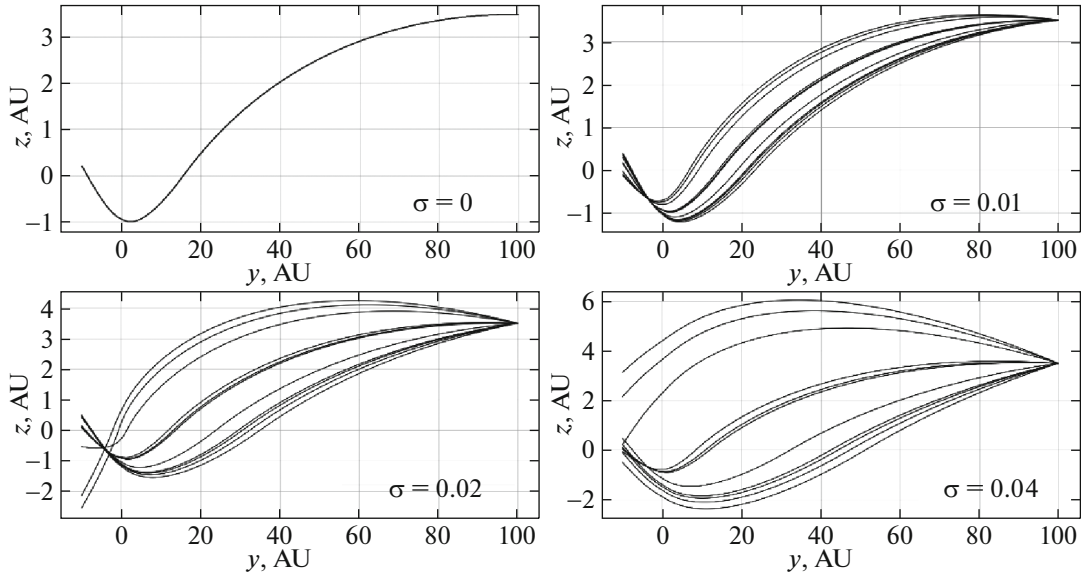
Fig. 9. Trajectories of particles originating from a small region on the boundary of the computational domain for different values of $\hat{\sigma}_z$. For non-zero dispersion particle trajectories are scattered, and no singularities appear. Radius of particles is 0.37 μm.
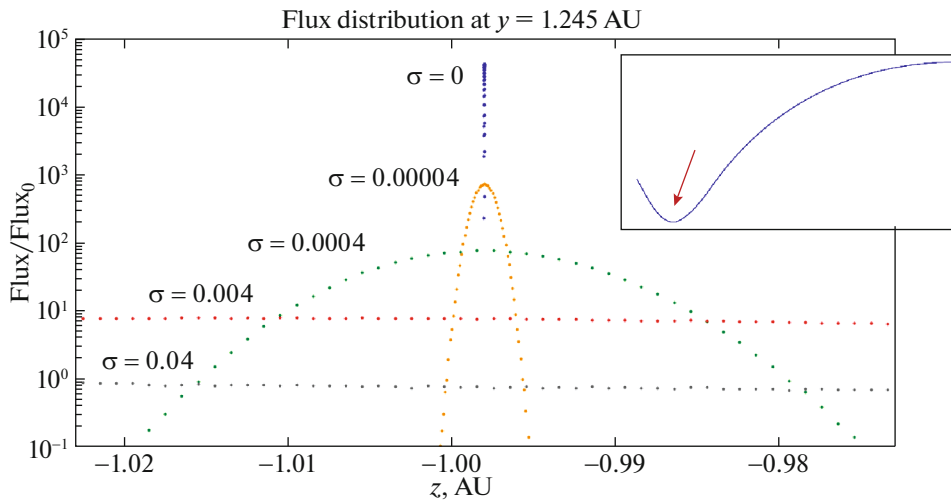

Fig. 10. Comparison of the fluxes carried by the ISD trajectories originating from a small region on the boundary of the computational domain with different dispersion $\hat{\sigma}_z$: 0, 0.00004, 0.0004, 0.004, 0.04. For each computation we have reached the convergence in cell size, Runge–Kutta integration steps and number of simulated particles. The maximal value of fluxes is approximately inversely proportional to the dispersion $\hat{\sigma}_z$. For the computation without dispersion the cell size in the z-axis direction is 10^{-6} (AU). Relative statistical error is limited by 5% at each point. Radius of particles is 0.37 μm.

0, 0.01, 0.02, 0.04. Figure 7 presents the density maps obtained for the four values of $\hat{\sigma}_z$. With increasing $\hat{\sigma}_z$ the density maxima are smeared and their singular-ities disappear. The regions of overdensity remain only in the vicinity of the HCS. This clumping up of dust particles is associated with an increase in the magnitude of the Lorentz force at small heliocentric distances, that leads to decrease of the particle oscillations around the HCS amplitude. Then, the gross tendency is for the ISD to converge to the HCS plane and so the regions of overdensity appear. In

Fig. 8 we can see how density at cells containing caustic points changes quantitatively with variation of $\hat{\sigma}_z = 0$. The small values of the dispersion of 4% in the boundary velocity distribution change the density distribution in the heliosphere drastically.

The reason for the disappearance of the singular-ities is clearly seen from Figs. 9, 10. Figure 9 shows trajectories of particles originating from a small re-gion on the outer boundary of the computational do-main for different $\hat{\sigma}_z$ values. As it was mentioned above, singularities appear where the width of the
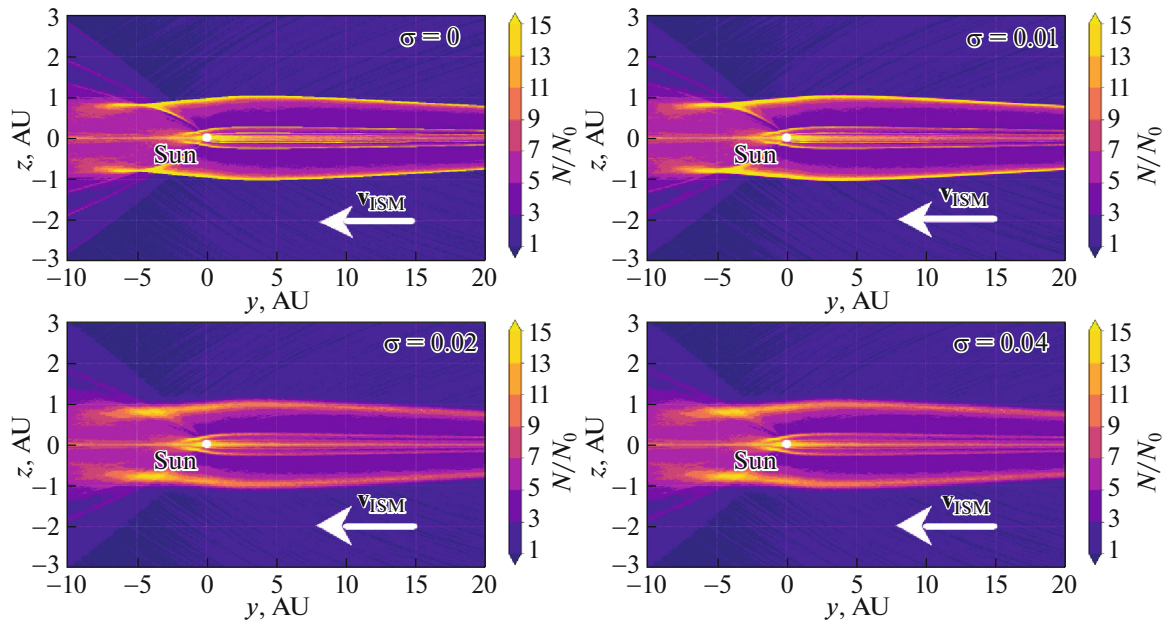
Fig. 11. Comparison of density map distributions with different dispersion of the v_y velocity component: 0, 0.01, 0.02, 0.04. The shape of the overdensity regions remains virtually unchanged with the variation in the dispersion. Relative statistical error is limited by 5−6% at each point. Number of trajectories $N = 200\,000$. Radius of particles is 0.37 μm.

flux tube approaches zero. For non-zero dispersion particle trajectories are scattered, and therefore no singularities appear. Density flux distributions in the vicinity of the point corresponding to the caustic at $\hat{\sigma}_z = 0$ by particles originating from a small region on the outer boundary are demonstrated on Fig. 10 for different $\hat{\sigma}_z$ values. One can appreciate that the maxima of these density flux distributions are approximately inversely proportional to the value of dispersion $\hat{\sigma}_z$. Thus even extremely small values of dispersion drastically influence the ISD distribution inside the heliosphere.

In order to study the influence of dispersion of the v_y velocity component on the density distribution we should use instead of the expression (11) the following boundary condition function:

$$f_{\mathrm{TS}}(\mathbf{v}) = n_{\mathrm{ISM}}\delta(v_x)\frac{1}{\sigma_y\sqrt{2\pi}}$$
$$\times \exp\left(-\frac{(v_y + v_{\mathrm{ISM}})^2}{2\sigma_y^2}\right)\delta(v_z), \qquad (24)$$

which in the dimensionless form is:

$$f_{\mathrm{TS}}(\hat{\mathbf{v}}) = \delta(\hat{v}_x)\frac{1}{\hat{\sigma}_y\sqrt{2\pi}}$$
$$\times \exp\left(-\frac{(\hat{v}_y + 1)^2}{2\hat{\sigma}_y^2}\right)\delta(\hat{v}_z). \qquad (25)$$

Figure 11 shows the comparison of density distributions for the cases with different values of dispersion $\hat{\sigma}_y$ of the v_y velocity component

($\hat{\sigma}_y$: $0, 0.01, 0.02, 0.04$). We can see that the shape of the overdensity region has remained virtually unchanged for the selected dispersion values. Since the same dispersion values were used previously for the v_z velocity component, one can conclude that the dispersion of the v_z velocity component has a greater impact on the density distribution than the dispersion of the v_y velocity component. This is because the regions of overdensity are stretched along Oy-axis and, therefore, in the stationary case small variations in the v_y velocity component cannot significantly affect the ISD density distribution.

CONCLUSIONS

In this paper we demonstrated that the singularities of the ISD density in the heliosphere, discovered using a Lagrangian approach in Mishchenko et al. (2020), can also be found by Monte-Carlo simulations. It requires super-small computational cells. In our calculations the required size of cell (in z-direction) is 10^{-3} AU Having such size of the cells in all domain computationally unrealistic. Weaker resolution (i.e., larger cells) does not allow the caustics to be found.

Dispersion was introduced as a normal distribution of one of the velocity component. It was shown that the density singularities are smeared due to the dispersion. The regions of overdensity are smoothed and remain only in the vicinity of the heliospheric current sheet. It is known (Hoang et al. 2012) that the

velocity dispersion can reach values of approximately 15% due to spatial and temporal inhomogeneities in the interstellar magnetic field. Significant qualitative and quantitative changes in the density distribution emerge even with 5% dispersion as it was shown. Thus, the velocity dispersion is an extremely important effect that strongly influences the ISD density distribution inside the heliosphere.

In the future we plan to develop our model to the case of a time-dependent solar magnetic field in accordance with the 22-year solar cycle (in this article we consider the solar magnetic field just in one focusing phase (Mann 2010) all the time). Certainly this is a highly important effect that has a major impact on the ISD density inside the heliosphere and which is necessary to take into consideration.

ACKNOWLEDGMENTS

REFERENCES

1. D. B. Alexashov, O. A. Katushkina, V. V. Izmodenov, and P. S. Akaev, Mon. Not. R. Astron. Soc. **458**, 2553 (2016).
2. N. Altobelli, S. Kempf, H. Krüger, M. Landgraf, M. Roy, and E. Grün, Journal of Geophysical Research **110**, 7102 (2005).
3. N. Altobelli, V. Dikarev, S. Kempf, R. Srama, S. Helfert, G. Moragas-Klostermeyer, M. Roy, and E. Grün, Journal of Geophysical Research **112**, 7105 (2007).
4. I. I. Baliukin, V. V. Izmodenov, E. Möbius, D. B. Alexashov, O. A. Katushkina, and H. Kucharek, Astrophys. J. **850**, 119 (2017).
5. J. L. Bertaux and J. E. Blamont, Astron. Astrophys. **11**, 200 (1971).
6. J. L. Bertaux and J. E. Blamont, Nature **262**, 263 (1976).
7. A. Czechowski and I. Mann, Astron. Astrophys. **410**, 165 (2003).
8. B. T. Draine, Space Sci. Rev. **143**, 333 (2009).
9. E. Grün, B. Gustafson, I. Mann, M. Baguhl, G. E. Morfull, P. Staubach, A. Taylor, and H. A. Zook, Astron. Astrophys. **286**, 915 (1994).
10. B. A. S. Gustafson, Ann. Rev. **22**, 553 (1994).
11. T. Hoang, A. Lazarian, and R. Schlickeiser, Astrophys. J. **747**, 54 (2012).
12. V. V. Izmodenov and D. B. Alexashov, Astrophys. J. Suppl. Ser. **220**, 32 (2015).
13. V. V. Izmodenov and D. B. Alexashov, Astron. Astrophys. **633**, 12 (2020).
14. V. V. Izmodenov, Y. G. Malama, A. P. Kalinin, M. Gruntman, R. Lallement, and I. P. Rodionova, Astrophys. Space Sci. **274**, 71 (2000).
15. O. A. Katushkina, V. V. Izmodenov, D. B. Alexashov, N. A. Schwadron, and D. J. McComas, Astrophys. J. Suppl. Ser. **220**, 33 (2015).
16. O. A. Katushkina, and V. V. Izmodenov, Mon. Not. R. Astron. Soc. **486**, 4947 (2019).
17. M. Landgraf, W. J. Baggaley, E. Grün, H. Krüger, and G. Linkert, J. Geophys. Res.: Space Phys. **105**, 10343 (2000).
18. M. Landgraf, H. Krüger, N. Altobelli, and E. Grün, J. Geophys. Res.: Space Phys. **108**, 8030 (2003).
19. E. H. Levy and J. R. Jokipii, Nature **264**, 423 (1976).
20. I. Mann, Annu. Rev. Astron. Astrophys **48**, 173 (2010).
21. J. S. Mathis, W. Rumpl, and K. H. Nordsieck, Astrophys. J. **217**, 425 (1977).
22. D. J. McComas, M. Bzowski, P. Frisch, S. A. Fuselier, M. A. Kubiak, H. Kucharek, T. Leonard, E. Möbius, et al., Astrophys. J. **801**, 28 (2015).
23. A. V. Mishchenko, E. A. Godenko, and V. V. Izmodenov, Mon. Not. R. Astron. Soc. **491**, 2808 (2020).
24. E. Moebius, P. Bochsler, M. Bzowski, G. B. Crew, H. O. Funsten, S. A. Fuselier, A. Ghielmetti, D. Heirtzler, et al., Science **326**, 969 (2009).
25. A. N. Osiptsov, Astrophys. Space Sci. **274**, 377 (2000).
26. N. V. Pogorelov, J. Heerikhuisen, G. P. Zank, S. N. Borovikov, P. C. Frisch, and D. J. McComas, Astrophys. J. **742**, 104 (2011).
27. E. Quémerais, B. R. Sandel, V. V. Izmodenov, and G. R. Gladstone, *Cross-Calibration of Far UV Spectra of Solar System Objects and the Heliosphere* **141** (2013).
28. J. D. Slavin, P. C. Frisch, H.-R. Müller, J. Heerikhuisen, N. V. Pogorelov, W. T. Reach, and G. P. Zank, Astrophys. J. **760**, 46 (2012).
29. V. J. Sterken, N. Altobelli, S. Kempf, G. Schwehm, R. Srama, and E. Grün, Astron. Astrophys. **538**, A102 (2012).
30. V. J. Sterken, A. J. Westphal, N. Altobelli, D. Malaspina, and F. Postberg, Space Sci. Rev. **215**, 7, 43 (2019).
31. P. Strub, H. Krüger, and V. J. Sterken, Astrophys. J. **812**, 140 (2015).
32. P. Strub, V. J. Sterken, R. Soja, H. Krüger, E. Grün, and R. Srama, Astron. Astrophys. **621**, A54 (2019).
33. M. Witte, H. Rosenbauer, E. Keppler, H. Fahr, P. Hemmerich, H. Lauche, A. Loidl, and R. Zwick, Astron. Astrophys. **92**, 333 (1992).
34. M. Witte, Astron. Astrophys. **426**, 835 (2004).
35. E. J. Zirnstein, J. Heerikhuisen, H. O. Funsten, G. Livadiotis, D. J. McComas, and N. V. Pogorelov, Astrophys. J., Lett. **818**, 30 (2016).

Translated by the authors